SYNTHESIS AND SINTERING 5 (2025) 323–331

Available online at www.synsint.com

Synthesis and Sintering

ISSN 2564-0186 (Print), **ISSN** 2564-0194 (Online)

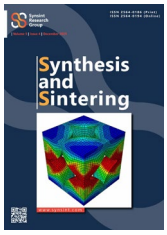

Research article

Porosity-dependent mechanical properties of sintered titanium: RVE-based finite element modeling and Gibson–Ashby analysis

Ata Khabaz-Aghdam [a,*], **Takunda Happison Nyenyewa** [b], **Jacob Kabole Kahungwa** [b], **Cengiz Mesut Bükeç** [c], **Halise Duygu Özalp** [d]

[a] *Department of Aeronautical Engineering, Faculty of Aviation and Space Sciences, University of Kyrenia, Kyrenia, Mersin 10, Turkey*
[b] *Department of Mechanical Engineering, Faculty of Engineering, University of Kyrenia, Mersin 10, Kyrenia, Turkey*
[c] *Department of Aviation Management, Faculty of Aviation and Space Sciences, University of Kyrenia, Kyrenia, Mersin 10, Turkey*
[d] *Department of Sociology, Başkent University, Ankara, Turkey*

A B S T R A C T

Porous sintered titanium structures are widely used in biomedical and lightweight engineering applications due to their tunable mechanical performance and favorable biocompatibility. In this study, the porosity-dependent mechanical behavior of sintered titanium is investigated using a three-dimensional representative volume element (RVE) combined with finite element modeling. The RVE is constructed from an ordered arrangement of spherical titanium particles under periodicity, and sintering-induced neck growth is represented geometrically by controlled interparticle overlap achieved through systematic reduction of the RVE size. Uniaxial displacement-controlled loading is applied to extract the homogenized stress–strain response over a range of porosity levels. The simulations demonstrate a strong sensitivity of the effective elastic modulus, yield strength, and energy absorption capacity to relative density and neck evolution. The effective mechanical properties are evaluated through homogenization and analyzed within the framework of Gibson–Ashby scaling. The normalized stiffness, strength, and absorbed energy exhibit clear power-law relationships with relative density, with scaling exponents consistent with values reported for sintered and cellular metallic materials. The results highlight the critical role of microstructural architecture and particle connectivity in governing stiffness degradation, strength reduction, and energy absorption during densification. Overall, the proposed RVE-based numerical framework provides a physically consistent and computationally efficient tool for predicting the effective mechanical response of sintered titanium as a function of porosity, offering valuable insights for the design and optimization of porous titanium components in biomedical and structural applications.

KEYWORDS

Sintered titanium
Representative volume element (RVE)
Finite element modeling (FEM)
Mechanical properties
Gibson–Ashby scaling laws

OPEN ACCESS

* Corresponding author. *E-mail address:* ata.khabazaghdam@kyrenia.edu.tr (A. Khabaz-Aghdam)
Received 1 December 2025; Received in revised form 26 December 2025; Accepted 26 December 2025.

https://doi.org/10.53063/synsint.2025.54317

1. Introduction

Porous and sintered titanium materials have attracted considerable attention in recent years due to their unique combination of low density, corrosion resistance, and favorable mechanical and biological properties. These characteristics make porous titanium particularly attractive for biomedical implants, lightweight structural components, and energy-absorbing applications, where tailoring stiffness, strength, and deformation behavior through controlled porosity is essential [1–3]. In such applications, the mechanical performance of the material is governed not only by the intrinsic properties of titanium but also by the microstructural architecture resulting from powder packing and sintering-induced neck formation.

The presence of porosity leads to a pronounced reduction in elastic modulus, yield strength, and energy absorption capacity compared to fully dense titanium. Classical approaches for describing this behavior often rely on empirical or semi-empirical scaling laws, among which the Gibson–Ashby model is the most widely adopted framework for cellular and porous solids [4, 5]. In this model, effective mechanical properties are expressed as power-law functions of relative density, with scaling exponents reflecting the dominant deformation mechanisms. While the Gibson–Ashby relations have been successfully applied to a wide range of foams and lattices, their direct application to sintered metallic materials remains challenging due to the complex role of interparticle neck growth, particle connectivity, and localized plasticity [6–8].

Experimental characterization of sintered titanium over a wide porosity range is often costly and time-consuming, and it provides limited insight into the local stress and strain distributions governing macroscopic behavior. As a result, numerical approaches based on representative volume elements (RVEs) have emerged as powerful tools for linking microstructural features to effective mechanical properties [9–11]. RVE-based finite element modeling enables explicit representation of particle geometry, interparticle contacts, and neck formation, allowing for systematic investigation of porosity effects while maintaining computational efficiency.

Several numerical studies have employed idealized RVEs composed of spherical particles to model sintered metals and powders [12–14]. However, many existing models either assume random particle arrangements without clear geometric control or neglect the evolution of neck geometry during sintering. In reality, sintering induces material transport at particle contacts, resulting in neck growth that significantly alters load transfer paths and deformation mechanisms. Accurately capturing this effect is essential for predicting the mechanical response of sintered titanium, particularly under elastic–plastic loading conditions.

In the present study, a three-dimensional RVE-based finite element framework is developed to investigate the porosity-dependent mechanical behavior of sintered commercially pure titanium (CP-Ti). The RVE consists of a periodic arrangement derived from eight spherical particles, where sintering is modeled through controlled geometric overlap that represents progressive neck growth. By systematically varying the center-to-center particle spacing, porosity levels ranging from approximately 40% to 19% are achieved. The effective elastic modulus, yield strength, Poisson's ratio, and energy absorption capacity are extracted from homogenized stress–strain responses obtained under uniaxial loading.

The numerical results are interpreted within the Gibson–Ashby scaling framework by evaluating pointwise scaling exponents for stiffness, strength, and absorbed energy as functions of relative density. Particular attention is given to the evolution of deformation mechanisms with densification, as revealed by stress and plastic strain localization in interparticle neck regions. By explicitly linking microstructural geometry, local deformation, and macroscopic scaling behavior, this study provides new insight into the mechanical response of sintered titanium and highlights the limitations of applying constant Gibson–Ashby exponents across broad porosity ranges.

The proposed modeling approach offers a physically consistent and predictive tool for assessing the mechanical performance of sintered titanium, with potential applications in the design and optimization of porous metallic components for biomedical and structural use.

2. Materials and methods

2.1. Titanium material properties

In the present numerical study, the solid phase of the sintered microstructure was assumed to consist of commercially pure titanium (CP-Ti). At the particle scale, titanium was modeled as an isotropic, homogeneous elastic–plastic material, representing the mechanical response of fully dense bulk titanium. This assumption is commonly adopted in micromechanical and RVE-based simulations of sintered and porous metals, where the effective behavior of the porous structure arises from geometric effects (porosity, neck morphology, and load-transfer paths) rather than degradation of the intrinsic material properties.

The elastic behavior of titanium was described using linear isotropic elasticity, characterized by Young's modulus (E) and Poisson's ratio (ν). Plastic deformation was modeled using an elastic–plastic constitutive law with isotropic hardening, with yielding defined by a von Mises yield criterion. A yield strength representative of high-strength commercially pure titanium was selected, consistent with values reported for CP-Ti grades 3–4 and powder-processed titanium materials.

The adopted material parameters are summarized in Table 1. These values fall within well-established ranges reported in the literature for bulk CP-Ti and are widely used in numerical simulations of titanium-based porous and sintered structures. By assigning bulk titanium properties at the particle level, the reduction in stiffness and strength observed in the simulations originates solely from microstructural features such as porosity, particle arrangement, and sintering neck geometry.

Table 1. Mechanical properties of commercially pure titanium used in the simulations.

Property	Symbol	Value	Unit	Ref.
Young's modulus	E	115	GPa	[15–17]
Poisson's ratio	ν	0.34	–	[15–17]
Yield strength	σ_y	380	MPa	[16, 18, 19]

2.2. Representative volume element (RVE)

In this study, a periodic, ordered RVE was employed to model the mechanical behavior of sintered titanium. The adopted RVE geometry is based on a regular arrangement of spherical titanium particles, which is well suited for isolating the influence of sintering-induced neck growth on effective mechanical properties.

The initial geometric configuration consists of eight identical spherical particles with radius r, positioned at the corners of a cubic domain (Fig. 1a). Due to periodicity, one-eighth of each spherical particle is geometrically associated with the RVE (Fig. 1b). In the reference configuration corresponding to particle contact without overlap, the total solid volume equals that of one complete sphere. For sintered configurations, interparticle overlap leads to an increase in solid volume due to neck formation. This configuration represents a periodic array of particles in mutual contact and ensures compatibility with periodic boundary conditions [20].

The representative volume element (RVE) is defined as a cubic domain of size L×L×L, where L corresponds to the center-to-center spacing between adjacent spherical particles. The particle radius R is kept constant throughout the study, and sintering is represented by progressively reducing the cube edge length L, which induces controlled geometric interpenetration between neighboring particles.

In the reference configuration corresponding to particles in point contact, the cube edge length is L=2R. Sintering is modeled by decreasing L below 2R, leading to symmetric particle infusion at each contact. For a given cube size L, the total overlap depth between two adjacent particles is 2R−L, with each particle contributing half of this value. For example, at L=1.9R, the total infusion depth is 0.1R, corresponding to an interpenetration of 0.05R from each particle.

This geometric approach provides a systematic means of representing sintering-induced neck growth while preserving periodicity and allowing direct control of the sintering level through the RVE size.

2.3. Modeling of sintering-induced neck growth

In the present study, sintering was modeled using a geometric interpenetration approach, in which neck formation between adjacent particles is represented by controlled overlap of spherical particles. The particle radius r was kept constant throughout all simulations, while the degree of sintering was governed by the size of the cubic RVE.

The cube edge length L, which is equal to the center-to-center spacing between neighboring particles, was systematically reduced from the reference value L=2R, corresponding to particles in point contact, to smaller values representing increasing sintering levels. Reduction of L below 2R induces symmetric interparticle infusion at each contact, leading to the formation of neck regions between adjacent particles.

For a given cube size L, the total overlap depth between two neighboring particles is given by:

$$\Delta = 2R - L \tag{1}$$

with each particle contributing an infusion depth of Δ/2. In the present work, the cube size was varied from L=1.9R to L=1.65R in increments of 0.05R, corresponding to total overlap depths ranging from 0.1R to 0.35R. This approach enables systematic investigation of the effect of neck growth on the mechanical response while preserving the ordered topology and periodicity of the microstructure.

2.4. Porosity definition and calculation (revised)

The porosity of the representative volume element was defined as the ratio of void volume to the total RVE volume and was evaluated for each sintering level based on the actual geometric configuration. Porosity ϕ is expressed as:

$$\phi = 1 - \frac{V_s}{V_{RVE}} \tag{2}$$

where V_s is the total volume of solid titanium contained within the RVE and $V_{RVE}=L^3$ is the volume of the cubic unit cell.

Unlike the reference configuration with particles in point contact, where the solid volume equals that of a single sphere, sintered configurations exhibit interparticle overlap that increases the solid volume due to neck formation. Consequently, the solid volume V_s is not constant and depends on the prescribed cube size L. For each sintering level, V_s was therefore obtained directly from the geometric model to accurately account for overlap-induced material transport.

The relative density ρ/ρ_s was calculated as:

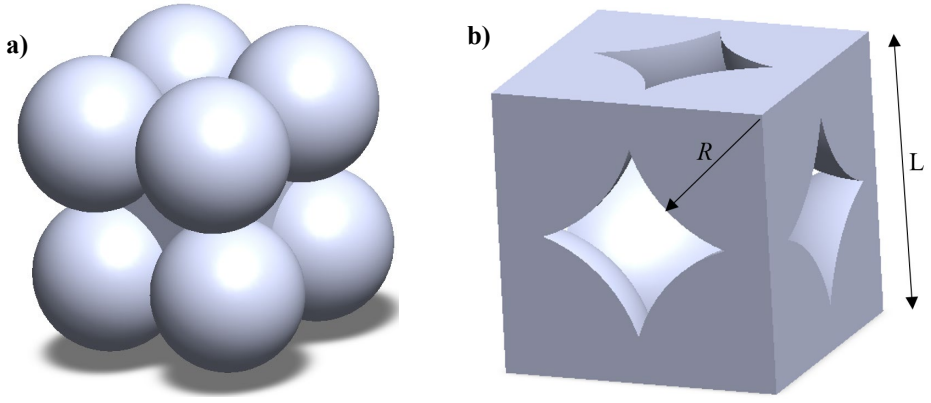

Fig. 1. a) Ordered arrangement of eight spherical particles, forming the geometric basis of the representative volume element (RVE). The particles are located at the corners of a cubic unit cell and are shown in contact or interpenetration, depending on the prescribed cube size, to represent different stages of sintering. b) Cubic representative volume element (RVE) constructed from one-eighth portions of eight spherical particles under periodic boundary conditions. The particle radius r remains constant, while the cube edge length L is varied to represent different sintering levels. Decreasing L results in symmetric particle infusion and growth of interparticle neck regions.

$$\frac{\rho}{\rho_s} = \frac{V_s}{L^3} \tag{3}$$

and the porosity was then determined as:

$$\phi = 1 - \frac{\rho}{\rho_s} \tag{4}$$

Using this procedure, porosity decreases monotonically as the cube size L is reduced, reflecting progressive densification and neck growth during sintering. This geometric-based evaluation ensures consistency between the RVE morphology and the computed effective mechanical properties.

2.5. Finite element model and boundary conditions

The representative volume element (RVE) was discretized using three-dimensional solid finite elements [21, 22]. A uniform mesh with a characteristic element size of 0.001 mm was employed throughout the RVE. This element size was selected based on a mesh convergence analysis to ensure accurate capture of the global mechanical response without the need for local mesh refinement.

As shown in Fig. 2, to represent the periodic nature of the ordered microstructure and to suppress rigid-body motion, symmetry boundary conditions were applied on the four lateral faces of the cubic RVE. Specifically, the displacement normal to each lateral face was constrained, while in-plane displacements were left unconstrained. This treatment enforces symmetry across the RVE boundaries and is consistent with a periodically repeated microstructure under uniaxial loading.

Mechanical loading was applied along the vertical direction. The bottom face of the RVE was constrained against displacement in the loading direction (y-direction), while the top face was subjected to a prescribed uniform displacement equal to 0.2L. All other displacement components on the top and bottom faces were left free to allow natural lateral deformation.

This boundary condition setup imposes a macroscopic uniaxial strain along the loading direction while allowing heterogeneous deformation within the RVE. The adopted loading scheme ensures stable numerical convergence and enables the extraction of the effective stress–strain response of the sintered microstructure.

2.6. Homogenization procedure and Gibson–Ashby scaling

The effective mechanical properties of the sintered titanium microstructure were obtained through a homogenization procedure based on the finite element response of the representative volume element (RVE). Macroscopic stress and strain measures were computed from the volume-averaged microscopic fields under uniaxial loading.

The macroscopic (homogenized) normal strain in the loading direction (y-direction) was defined as [23]:

$$\varepsilon_{yy} = \frac{\Delta u_y}{L} \tag{5}$$

where Δu_y is the prescribed displacement applied to the top face of the RVE and L is the cube edge length. The macroscopic normal stress was calculated from the reaction force on the constrained bottom face as:

$$\sigma_{yy} = \frac{F_y}{A} \tag{6}$$

where F_y is the total reaction force in the loading direction and $A = L^2$ is the cross-sectional area of the RVE.

The effective Young's modulus of the sintered microstructure, E_{eff}, was determined from the slope of the initial linear portion of the homogenized stress–strain curve:

$$E_{eff} = \frac{d\sigma_{yy}}{d\varepsilon_{yy}} \tag{7}$$

To enable comparison across different sintering levels, the effective mechanical properties were normalized by the corresponding properties of fully dense titanium. Specifically, the effective Young's modulus E_{eff}, yield strength $\sigma_{y,eff}$, and absorbed energy W_{eff} were normalized by the elastic modulus E_s, yield strength σ_y, and energy absorption capacity W_s of dense titanium, respectively.

The dependence of the normalized stiffness, strength, and energy absorption on relative density was analyzed within the framework of the Gibson–Ashby scaling law, expressed in its simplified form as [5]:

$$\frac{P_{eff}}{P_s} = \left(\frac{\rho}{\rho_s}\right)^n \tag{8}$$

where P denotes the mechanical property of interest (E, σ_y, or W), and n is a structure-dependent scaling exponent reflecting the dominant deformation and load-transfer mechanisms.

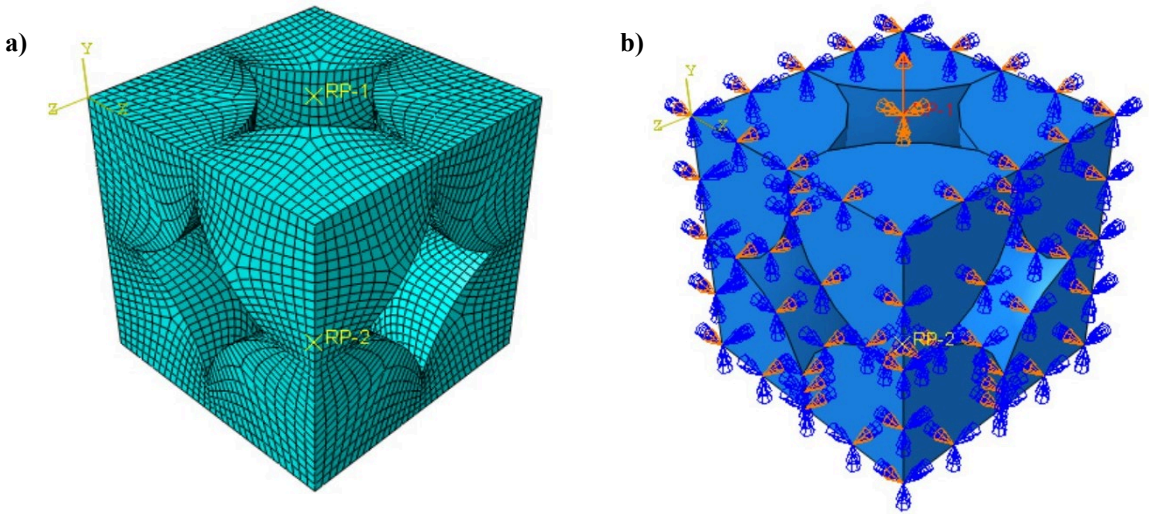

Fig. 2. a) Meshed RVE and b) boundary conditions and loading.

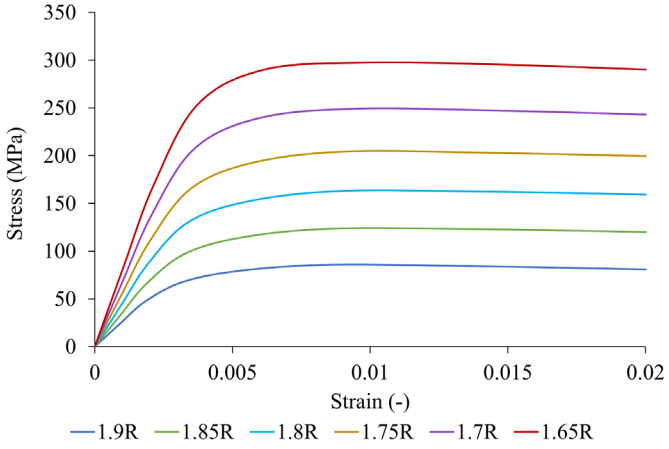

Fig. 3. Stress–strain curves of sintered CP-Ti obtained from finite element simulations of representative volume elements (RVEs) with different porosity levels, corresponding to varying cubic RVE sizes.

In the present study, the prefactor commonly introduced in the classical Gibson–Ashby formulation was taken as unity in order to focus on the scaling exponent *n*. This approach allows direct assessment of whether the numerically predicted evolution of stiffness, strength, and energy absorption with progressive densification follows classical scaling trends observed in cellular and sintered solids, without introducing additional fitting parameters.

3. Results and discussion

3.1. Mechanical response from finite element stress–strain analysis

The mechanical response of sintered titanium with different porosity levels was evaluated based on the homogenized stress–strain curves obtained from finite element simulations. Fig. 3 presents the stress–strain behavior of representative volume elements (RVEs) with porosity values ranging from 39.6% to 18.9%, corresponding to different sintering levels. The effective mechanical properties extracted from these curves—including Young's modulus, yield strength, and absorbed energy—are summarized in Table 2.

As shown in Fig. 3, the stress–strain curves exhibit a clear dependence on porosity. A pronounced increase in stiffness and load-carrying capacity is observed as porosity decreases, reflecting enhanced particle connectivity and progressive neck growth between adjacent particles. At high porosity levels (e.g., 39.6%), the material exhibits a relatively compliant response with a lower initial slope and early yielding. In contrast, specimens with lower porosity display a steeper elastic slope and a substantially higher stress level before yielding.

Quantitatively, the effective Young's modulus increases monotonically from 26.3 GPa at 39.6% porosity to 80.2 GPa at 18.9% porosity, representing more than a threefold increase as densification progresses. A similar trend is observed for the yield strength, which rises from 77.7 MPa to 280.4 MPa over the same porosity range. This pronounced strengthening effect highlights the dominant role of interparticle neck formation in facilitating load transfer and reducing stress concentrations within the porous network.

The energy absorption capacity, calculated as the area under the homogenized stress–strain curve up to a prescribed strain level of 0.02, also exhibits a strong sensitivity to porosity. This strain limit was selected to ensure consistent comparison across different sintering levels and to capture the mechanical work absorbed prior to significant plastic deformation. As shown in Table 2, the absorbed energy increases from 1.50 MPa at the highest porosity to 5.26 MPa at the lowest porosity. This enhancement reflects the combined effect of increased stiffness and higher yield stress in denser microstructures, enabling the material to sustain greater mechanical work within the specified strain range.

Table 2. Effective mechanical properties of sintered CP-Ti with different porosity levels obtained from finite element simulations of the representative volume element (RVE).

D	Porosity (%)	Young's Modulus, E_{eff} (GPa)	Yield strength, $\sigma_{y,eff}$ (MPa)	Energy absorbed, U_{eff} (MPa or MJ/m^3)	Poisson ratio, ν_{eff}
1.9R	39.6	26.3	77.72	1.504	0.0639
1.85R	35.5	35.5	112.75	2.178	0.0659
1.8R	31.3	45.4	149.22	2.870	0.0675
1.75R	27.1	56.0	188.00	3.594	0.0664
1.7R	22.9	67.6	232.33	4.393	0.0652
1.65R	18.9	80.2	280.43	5.257	0.0659

The effective Poisson's ratio obtained from the homogenized stress–strain response of the RVEs is summarized in Table 2. Over the investigated porosity range (18.9–39.6%), the effective Poisson's ratio remains low, with values between 0.064 and 0.068. Compared to fully dense titanium ($\nu \approx 0.34$), the porous microstructures exhibit a significantly reduced lateral-to-axial strain ratio. A slight increase in Poisson's ratio is observed as porosity decreases from 39.6% to 31.3%, followed by small oscillations around an approximately constant value for lower porosity levels.

The effective Poisson's ratio of the sintered titanium RVEs is significantly lower than that of fully dense titanium and remains nearly constant over the investigated porosity range. This behavior indicates that deformation is governed primarily by bending and rotation of interparticle necks rather than axial stretching of a continuous solid matrix. As porosity decreases, a slight increase in Poisson's ratio is initially observed due to enhanced particle connectivity and load transfer. However, beyond a relative density corresponding to approximately 31% porosity, the deformation mechanism remains bending-dominated, leading to a saturation of lateral strain response and only minor fluctuations in Poisson's ratio. Consequently, Poisson's ratio exhibits limited sensitivity to porosity compared to stiffness and strength.

The low and weakly porosity-dependent Poisson's ratio reflects bending-dominated deformation in the sintered particle network and confirms that lateral strain plays a secondary role in the effective mechanical response.

3.2. Stress distribution and local plastic deformation

Fig. 4 illustrates the von Mises stress distribution within the RVEs at an applied macroscopic strain of 0.02, corresponding to the onset of plastic deformation in the homogenized stress–strain response. At this strain level, the necking volume in all RVEs has entered the plastic regime, allowing a direct comparison of stress localization patterns across different porosity levels.

For all porosity configurations, the highest stress concentrations are observed in the interparticle neck regions. These necking zones act as primary load-bearing paths within the porous microstructure and therefore experience elevated local stresses. As a result, plastic yielding initiates preferentially in these regions, while the particle cores remain largely elastic at the same macroscopic strain. This behavior confirms that plastic deformation in sintered titanium is governed by localized stress amplification at particle contacts rather than uniform yielding of the solid phase.

As porosity decreases—equivalently, as the degree of interparticle overlap and neck size increases—the extent of the plastically deformed regions within the necks becomes more pronounced. Larger and more developed necks provide increased load-transfer area, which leads to higher overall stress levels and a broader distribution of plastic strain within these zones. Consequently, the plastic regions expand spatially with decreasing porosity, indicating a progressive transition from highly localized yielding toward more distributed plastic deformation within the load-bearing network.

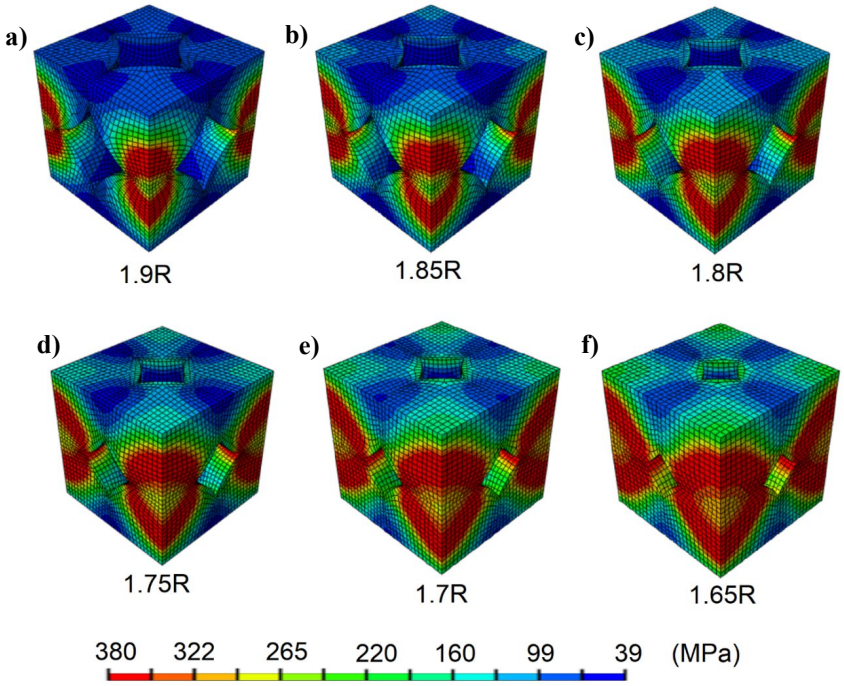

Fig. 4. Von Mises stress distribution in the representative volume elements (RVEs) at an applied macroscopic strain of 0.02 for different sintering levels, corresponding to center-to-center distances of a) 1.9R, b) 1.85R, c) 1.8R, d) 1.75R, e) 1.7R, and f) 1.65R. In all cases, stress localization is predominantly observed in the interparticle neck regions, where plastic deformation initiates. With decreasing porosity (increasing neck size), the extent and intensity of the plastically deformed zones increase, indicating enhanced load transfer through the necked particle network.

Table 3. Porosity, relative density, and Gibson–Ashby scaling of the effective elastic modulus of sintered titanium obtained from finite element simulations.

D	Porosity, ϕ (%)	$\frac{\rho}{\rho_s} = (1 - \phi)$	Young's modulus of RVE, E_{eff} (GPa)	Young's modulus of solid titanium, E_s (GPa)	E_{eff}/E_S	n_E, $(E_{eff} / E_s = (\rho / \rho_s)^{n_E})$
1.9R	39.6	0.604	26.3	115	0.2287	2.926
1.85R	35.5	0.645	35.5	115	0.3087	2.681
1.8R	31.3	0.687	45.4	115	0.3957	2.476
1.75R	27.1	0.729	56.0	115	0.4870	2.277
1.7R	22.9	0.771	67.6	115	0.5878	2.043
1.65R	18.9	0.811	80.2	115	0.6974	1.720

Despite the higher stiffness and strength of denser RVEs, the more porous configurations exhibit larger local strain levels at the same applied macroscopic strain. This behavior arises from the bending-dominated deformation mechanisms characteristic of porous microstructures, where axial loading is accommodated through localized rotations and bending of necks. In contrast, RVEs with lower porosity display a more constrained deformation response due to enhanced connectivity, resulting in higher stress levels but reduced local strain compared to their more porous counterparts.

Overall, the stress distribution results highlight the critical role of interparticle neck geometry in controlling both the initiation and evolution of plastic deformation in sintered titanium. The observed increase in plastic zone size with decreasing porosity provides a microstructural explanation for the monotonic increase in effective stiffness, yield strength, and energy absorption capacity reported in the preceding sections.

3.3. Gibson–Ashby predictions

The applicability of the Gibson–Ashby scaling framework to the numerically predicted mechanical behavior of sintered titanium was evaluated by analyzing the dependence of elastic modulus, yield strength, and energy absorption on relative density. Three separate scaling relations were considered, corresponding to elastic stiffness, plastic strength, and absorbed energy density, respectively. The results are summarized in Tables 3–5.

3.3.1. Elastic modulus scaling

Table 3 presents the normalized elastic modulus of the RVEs, E_{eff}/E_s, as a function of relative density, where E_s=115 GPa is the elastic modulus of fully dense titanium. For each porosity level, the Gibson–Ashby exponent n_E was calculated directly from the power-law relation $E_{eff}/E_s = (\rho/\rho_s)^{n_E}$. The extracted values of n_E decrease systematically from 2.93 at the highest porosity (39.6%) to 1.72 at the lowest porosity (18.9%).

This trend indicates that the sensitivity of elastic stiffness to porosity diminishes with progressive densification. At high porosity, load transfer is strongly influenced by bending of slender interparticle necks, leading to a pronounced reduction in stiffness and higher scaling exponents. As porosity decreases and neck size increases, the load-bearing network becomes more efficient, resulting in a reduced dependence of stiffness on relative density.

3.3.2. Yield strength scaling

Table 4 summarizes the normalized yield strength $\sigma_{y,eff}/\sigma_{y,s}$, where $\sigma_{y,s}$ =380 MPa corresponds to the yield strength of fully dense titanium. The corresponding Gibson–Ashby exponent n_σ follows a similar decreasing trend, ranging from 3.15 at high porosity to 1.45 at low porosity.

The larger values of n_σ at high porosity reflect highly localized yielding within thin interparticle necks, where stress concentrations dominate the onset of plastic deformation. With increasing densification, plastic deformation becomes more distributed across the interconnected particle network, reducing the sensitivity of yield strength to further increases in relative density. This behavior is consistent with the observed expansion of plastic zones in the stress distribution analysis.

Table 4. Porosity, relative density, and Gibson–Ashby scaling of the effective yield strength of sintered titanium.

D	Porosity, ϕ (%)	$\frac{\rho}{\rho_s} = (1 - \phi)$	Yield strength of RVE, $\sigma_{y,eff}$ (MPa)	Yield strength of solid titanium, $\sigma_{y,s}$ (MPa)	$\sigma_{eff} / \sigma_{y,s}$	n_σ, $(\sigma_{eff} / \sigma_{y,s} = (\rho / \rho_s)^{n_\sigma})$
1.9R	39.6	0.604	77.72	380	0.205	3.148
1.85R	35.5	0.645	112.75	380	0.297	2.771
1.8R	31.3	0.687	149.22	380	0.393	2.490
1.75R	27.1	0.729	188.00	380	0.495	2.226
1.7R	22.9	0.771	232.33	380	0.611	1.892
1.65R	18.9	0.811	280.43	380	0.738	1.450

Table 5. Porosity, relative density, and Gibson–Ashby scaling of the absorbed energy density of sintered titanium.

D	Porosity, ϕ (%)	$\frac{\rho}{\rho_s} = (1 - \phi)$	Energy absorbed of RVE, U_{eff} (MPa, or MJ/m^3)	Yield strength of RVE, U_s (MPa)	U_{eff}/U_s	n_U, $(U_{eff} / U_s = (\rho / \rho_s)^{n_U})$
1.9R	39.6	0.604	1.504	6.972	0.216	3.042
1.85R	35.5	0.645	2.178	6.972	0.312	2.653
1.8R	31.3	0.687	2.870	6.972	0.412	2.364
1.75R	27.1	0.729	3.594	6.972	0.516	2.096
1.7R	22.9	0.771	4.393	6.972	0.630	1.776
1.65R	18.9	0.811	5.257	6.972	0.754	1.348

3.3.3. Energy absorption scaling

Table 5 reports the normalized absorbed energy density U_{eff}/U_s , where U_s=6.972 MPa represents the strain energy density of fully dense titanium modeled as an elastic–perfectly plastic material up to a strain of 0.02. The Gibson–Ashby exponent for energy absorption, n_U, decreases from 3.04 at high porosity to 1.35 at low porosity.

Because energy absorption integrates both elastic storage and plastic dissipation, its scaling behavior reflects the combined influence of stiffness and strength. At high porosity, inefficient load transfer and localized deformation limit energy absorption, resulting in high scaling exponents. As densification progresses, enhanced neck growth promotes more uniform plastic deformation and increased energy dissipation, reducing the dependence of absorbed energy on relative density.

Across all three properties, the Gibson–Ashby exponents exhibit a consistent and systematic decrease with decreasing porosity. This observation indicates that a single universal exponent cannot fully describe the mechanical response of sintered titanium over the entire porosity range. Instead, the effective scaling behavior evolves with microstructural densification, reflecting a transition from bending-dominated deformation at high porosity to more efficient, neck-controlled load transfer at lower porosity.

Moreover, the hierarchy of the extracted exponents ($n_E > n_U > n_\sigma$) highlights the distinct physical mechanisms governing elastic stiffness, plastic yielding, and energy absorption. While elastic modulus is most sensitive to porosity due to geometric load-bearing constraints, yield strength and energy absorption progressively benefit from enhanced interparticle connectivity and distributed plastic deformation.

Overall, the Gibson–Ashby framework provides a valuable reference for interpreting the numerically predicted trends, while the variation of the scaling exponents emphasizes the critical role of evolving microstructural architecture in sintered titanium. These results demonstrate that porosity-dependent mechanical behavior cannot be fully captured by idealized foam models and must account for sintering-induced neck growth and particle-level deformation mechanisms.

4. Conclusions

This study presented a three-dimensional finite element homogenization framework to investigate the porosity-dependent mechanical behavior of sintered titanium based on representative volume element (RVE) modeling. By explicitly accounting for sintering-induced interparticle neck growth through controlled geometric overlap, the approach enables a direct link between microstructural architecture and effective mechanical response.

The numerical results demonstrated that porosity has a pronounced influence on elastic stiffness, yield strength, and energy absorption capacity. All three properties increase monotonically with decreasing porosity, reflecting enhanced load transfer through enlarged interparticle necks. Stress and plastic strain distributions revealed that deformation and yielding initiate preferentially within neck regions, confirming that mechanical response is governed by localized stress concentration and progressive neck-controlled plasticity rather than uniform deformation of the particle cores.

A systematic evaluation of the Gibson–Ashby scaling relations showed that the effective scaling exponents for elastic modulus, yield strength, and absorbed energy are not constant but decrease with increasing relative density. This behavior indicates an evolution of the dominant deformation mechanisms with densification, transitioning from bending-dominated responses at high porosity to more efficient, distributed load transfer at lower porosity. The hierarchy of the extracted exponents further highlights the distinct physical origins of stiffness, strength, and energy absorption in sintered titanium.

The effective Poisson's ratio of the porous RVEs was found to be significantly lower than that of fully dense titanium and only weakly dependent on porosity, indicating that lateral deformation plays a secondary role compared to axial load-bearing mechanisms over the investigated porosity range.

Overall, the proposed RVE-based framework provides a physically consistent and computationally efficient tool for predicting the mechanical behavior of sintered titanium as a function of porosity. The results emphasize the importance of explicitly modeling interparticle neck geometry when assessing the mechanical performance of sintered metals and offer valuable insight for the design and optimization of porous titanium components in structural and biomedical applications.

CRediT authorship contribution statement

Ata Khabaz-Aghdam: Conceptualization; Methodology; Project administration; Software; Supervision; Writing – original draft; Writing – review & editing.

Takunda Happison Nyenyewa: Data curation; Investigation; Software; Writing – original draft.

Jacob Kabole Kahungwa: Data curation; Investigation; Writing – original draft.

Cengiz Mesut Bükeç: Supervision; Writing – review & editing.

Halise Duygu Özalp: Supervision; Writing – original draft; Writing – review & editing.

Data availability

The data underlying this article will be shared on reasonable request to the corresponding author.

Declaration of competing interest

The authors declare no competing interests.

Funding and acknowledgment

The authors would like to express their sincere appreciation to the Aviation Management Department and the Mechanical Engineering Department of Kyrenia University for their valuable support, cooperation, and contributions throughout the course of this study.

References

[1] G.E. Ryan, A.S. Pandit, D.P. Apatsidis, Porous titanium scaffolds fabricated using a rapid prototyping and powder metallurgy technique, Biomaterials. 29 (2008) 3625–3635. https://doi.org/10.1016/j.biomaterials.2008.05.032.

[2] G.T. El-Bassyouni, S.M. Mouneir, A.M. El-Shamy, Advances in surface modifications of titanium and its alloys: implications for biomedical and pharmaceutical applications, Multiscale Multidiscip. Model. Exp. Des. 8 (2025) 265. https://doi.org/10.1007/s41939-025-00823-1.

[3] R. Rahmani, S.I. Lopes, K.G. Prashanth, Selective laser melting and spark plasma sintering: a perspective on functional biomaterials, J. Funct. Biomater. 14 (2025) 521. https://doi.org/10.3390/jfb14100521.

[4] C. Aguilar, I. Alfonso, D. González, E. Pio, G.O. Neves, et al., Simulation of the Influence of the Radial Graded Porosity Distribution on Elastic Modulus of γ/β Phase Ti-Based Alloy Foams for Bone Implant, Materials. 16 (2023) 7320. https://doi.org/10.3390/ma16237320.

[5] M.F. Ashby, The properties of foams and lattices, Philos. Trans. A: Math. Phys. Eng. Sci. 364 (2006) 15–30. https://doi.org/10.1098/rsta.2005.1678.

[6] O.B. Olurin, N.A. Fleck, M.F. Ashby, Deformation and fracture of aluminium foams, Mater. Sci. Eng: A. 291 (2000) 136–146. https://doi.org/10.1016/S0921-5093(00)00954-0.

[7] A.P. Roberts, Statistical reconstruction of three-dimensional porous media from two-dimensional images, Phys. Rev. 56 (1997) 3203. https://doi.org/10.1103/PhysRevE.56.3203.

[8] M. Doroszko, A. Seweryn, Pore-scale numerical modelling of large deformation behaviour of sintered porous metals under compression using computed microtomography, Mech. Mater. 141 (2020) 103259. https://doi.org/10.1016/j.mechmat.2019.103259.

[9] V. Kouznetsova, W.A. Brekelmans, F. Baaijens, An approach to micro-macro modeling of heterogeneous materials, Comput. Mech. 27 (2001) 37–48. https://doi.org/10.1007/s004660000212.

[10] M.G. Geers, V.G. Kouznetsova, W. Brekelmans, Multi-scale computational homogenization: Trends and challenges, J. Comput. Appl. Math. 234 (2010) 2175–2182. https://doi.org/10.1016/j.cam.2009.08.077.

[11] T. Kanit, S. Forest, I. Galliet, V. Mounoury, D. Jeulin, Determination of the size of the representative volume element for random composites: statistical and numerical approach, Int. J. Solids Struct. 40 (2003) 3647–3679. https://doi.org/10.1016/S0020-7683(03)00143-4.

[12] P. Raghavan, S. Ghosh, Concurrent multi-scale analysis of elastic composites by a multi-level computational model, Comput. Methods Appl. Mech. Eng. 193 (2004) 497–538. https://doi.org/10.1016/j.cma.2003.10.007.

[13] H.X. Zhu, J.F. Knott, N.J. Mills, Analysis of the elastic properties of open-cell foams with tetrakaidecahedral cells, J. Mech. Phys. Solids. 45 (1997) 319–343. https://doi.org/10.1016/S0022-5096(96)00090-7.

[14] O.M. Ibrahim, A.H. Al-Saiafi, S. Alotaibi, Thermal conductivity of porous sintered metal powder and the Langmuir shape factor, Heat Mass Transf. 57 (2021) 1289–1304. https://doi.org/10.1007/s00231-021-03032-x.

[15] J.R. Davis, Handbook of materials for medical devices, ASM Int. (2003).

[16] Q. Chen, G.A. Thouas, Metallic implant biomaterials, Mater. Sci. Eng. R: Rep. 87 (2015) 1–57. https://doi.org/10.1016/j.mser.2014.10.001.

[17] M. Niinomi, Mechanical properties of biomedical titanium alloys, Mater. Sci. Eng: A. 243 (1998) 231–236. https://doi.org/10.1016/S0921-5093(97)00806-X.

[18] R. Mahmoodian, N.S.M. Annuar, G. Faraji, N.D. Bahar, B.A. Razak, M. Sparham, Severe plastic deformation of commercial pure titanium (CP-Ti) for biomedical applications: a brief review, JOM. 71 (2019) 256–263. https://doi.org/10.1007/s11837-017-2672-4.

[19] L.C. Zhang, L.Y. Chen, A review on biomedical titanium alloys: recent progress and prospect, Adv. Eng. Mater. 21 (2019) 1801215. https://doi.org/10.1002/adem.201801215.

[20] A. Basalah, S. Esmaeili, E. Toyserkani, On the influence of sintering protocols and layer thickness on the physical and mechanical properties of additive manufactured titanium porous bio-structures, J. Mater. Process. Technol. 238 (2016) 341–351. https://doi.org/10.1016/j.jmatprotec.2016.07.037.

[21] J. Cao, A. Es'haghioskui, P. Dong, Z. Gong, H. Yuan, Mechanical simulation and debonding risk analysis of OLED panels with optically clear adhesives, Displays. 83 (2024) 102722. https://doi.org/10.1016/j.displa.2024.102722.

[22] A.E. Oskui, M. Ebrahimi, S. Attarilar, Q. Wang, N. Choupani, F. Djavanroodi, On the Development of a Testing Device for Fracture Characterization under Mixed-Mode Loading Conditions, Advances in Accelerated Testing and Predictive Methods in Creep, Fatigue, and Environmental Cracking, ASTM Int. (2023) 127–140. https://doi.org/10.1520/STP164320210083.

[23] G. Costanza, D. Solaiyappan, M.E. Tata, Properties, applications and recent developments of cellular solid materials: A review, Materials. 16 (2023) 7076. https://doi.org/10.3390/ma16227076.